Electrochimica Acta 512 (2025) 145489

Contents lists available at ScienceDirect

Electrochimica Acta

journal homepage: www.journals.elsevier.com/electrochimica-acta

In situ UV–Vis absorption spectroscopy study of the water electrooxidation on cobalt oxide catalysts

Jia Du [a,*], Joaquín Morales-Santelices [a], Omeshwari Yadorao Bisen [a,b], Denis Antipin [a], Dulce M. Morales [a,c], Marcel Risch [a,*]

[a] Nachwuchsgruppe Gestaltung des Sauerstoffentwicklungsmechanismus, Helmholtz–Zentrum Berlin für Materialien und Energie GmbH, Hahn-Meitner Platz 1, Berlin 14109, Germany
[b] Institute of Materials Physics, University of Göttingen, Friedrich-Hund-Platz 1, Göttingen 37077, Germany
[c] Engineering and Technology Institute Groningen (ENTEG), University of Groningen, Nijenborgh 3, Groningen 9747 AG, the Netherlands

ARTICLE INFO

Keywords:
Oxygen evolution reaction
Cobalt electrocatalysts
In situ UV–Vis spectroscopy
Alkaline electrolyzer

ABSTRACT

Despite the current prominence of cobalt oxides as electrocatalysts for the alkaline oxygen evolution reaction (OER), there is a lack of unambiguous demonstration for the presence and the role of Co^{4+} prior to/during the OER. Here, we combine electrochemistry with in situ UV–Vis absorption spectroscopy to investigate and discuss the previously unaddressed effect of different OH^- concentrations in the range from 1 M to 0.016 M on the population of Co^{4+} in thin films of CoO_x and its concomitant impact on their OER performance. Evidence for Co^{4+} is provided by in-situ X-ray absorption spectroscopy. Our UV–Vis absorption spectroscopic findings indicate that, not only can the overall redox conversion of Co be qualitatively monitored as a function of potential and OH^- concentration, but also the formation of oxidized Co (i.e.,Co^{3+} and Co^{4+}) assigned to a peak at 800 nm can be more quantitatively tracked in situ via stepped potential spectroelectrochemistry; with their optical signals becoming stronger at higher OH^-concentrations above 1.2 V vs. RHE, which is consistent with voltammetric redox couples, indicating an enhancement in Co oxidation state and the consequent predominance of Co^{4+} under conditions of elevated OH^- concentrations. Furthermore, the evolved oxygen due to OER does not depend on Co^{4+} or OH^- activity at 1.54 V vs. RHE, while a correlation with both Co^{4+} and OH^- is identified at 1.59 V vs. RHE. This study not only provides spectral insight into the redox chemistry of Co at OER-relevant potentials but also highlights the importance of Co^{4+} in facilitating the alkaline OER at high OH^- concentrations and current densities.

1. Introduction

The quest for sustainable energy sources has initiated intensive research into the electrocatalytic water splitting reaction [1,2], which holds promise for green hydrogen production[2,3]. In this pursuit, the associated anodic oxygen evolution reaction (OER) has drawn significant attention due to its sluggish kinetics during water electrooxidation [4,5], consequently, the development of efficient catalysts is imperative to surmount this energy barrier [5,6]. Although Ru and Ir-based materials are regarded as superior OER electrocatalysts [7–9], their scarcity renders them impractical for widespread use in large-scale applications [9,10]. Co, by comparison, is earth-abundant and cost-effective, and its oxides show competitive OER activity in neutral and alkaline environments [11–13]. As a result, substantial endeavours have been undertaken to track alterations in compositions and structures of Co oxides under dynamic OER conditions [14], this includes changes in applied potentials and local environments, such as the change in pH (or OH^- concentration). These comprehensive studies have elucidated influences on the OER performance from the aforementioned experimental dynamics [14].

Another dynamic parameter is the oxidation state of Co. Metallic Co undergoes continuous conversion to form CoO, $Co(OH)_2$, $CoO_2H_{1.5}{\cdot}0.5H_2O$, Co_3O_4, CoOOH, CoO_2, etc. upon application of corresponding potentials[15–18]. This fact highlights the importance of determining the active oxidation states of Co towards the OER, which plays an equally important role in regulating the OER performance as the composition and structure do, since different oxidation states are associated with different limiting states of water electrooxidation[19].

* Corresponding authors.
E-mail addresses: jia.du@epfl.ch (J. Du), marcel.risch@helmholtz-berlin.de (M. Risch).

https://doi.org/10.1016/j.electacta.2024.145489
Received 24 July 2024; Received in revised form 15 November 2024; Accepted 7 December 2024
Available online 8 December 2024

An in situ Raman spectroscopy study on CoO_x film revealed that Co^{4+} could form at 1.58V_{RHE}[23], and concluded that the enhancement in OER activity is attributed to the increased population of surface Co^{4+}. Similarly, the electrodeposited $Co(OH)_2$ film was studied [26]. Their findings showed that $Co^{>3+}$ is formed at 1.63 V_{RHE}, which suggests that a portion of Co has been converted from 3+ to 4+. A wide electrolyte pH spanning from 0 to 14 was also employed for the study of electrodeposited CoO_x film[27] showing that Co^{4+} serves as a partial resting species and its formation precedes the OER. A model CoO_x catalyst comprising Co_3O_4 and CoO showed Co^{4+}=*O* at 1.4 V_{RHE}, which highlights its key role in modulating the OER performance[22]. A similar study carried out on the mixed $Co(OH)_2$—Co_3O_4 catalyst and demonstrated the presence of Co^{4+} at OER potentials[28]. These findings suggest the importance of biphasic Co oxide catalysts in facilitating the formation of Co^{4+}, which actively participates in the OER cycle. Moreover, Co^{4+} was detected under neutral pH conditions[25,32]. All these preceding findings suggest the presence and the potential advantages of Co^{4+} during water electrooxidation. Yet, it must be noted that other studies did not find Co^{4+} (Table 1), so that its role for the OER is still actively disputed.

The oxidation states of Co are interrelated with their dynamic compositions and structures, which means that changes in composition or structure may lead to changes in oxidation state, and vice versa. All of this complicates the system under study and necessitates the use of in situ/ operando techniques that are able to track the system under dynamic operation conditions. Among all the in situ/operando methods, UV–Vis absorption spectroelectrochemistry stands out as a spectroscopic technique for its simplicity and accessibility to most research laboratories[29,30], which has been successfully employed in several preceding studies to monitor the valence changes of transition metal oxides during the OER[31–33].

Motivated by previous findings, herein, we choose to study amorphous CoO_x prepared via electrodeposition[34]. Catalysts prepared via similar methods do not show significant local structural changes during the OER[24], which largely isolates the study of the Co oxidation state. We use in situ UV–Vis absorption spectroscopy to track the evolution of Co oxidation state induced by changing the applied potentials and electrolyte pH, and identify the presence of Co^{4+} in alkaline OER.

2. Experimental

2.1. Chemicals and materials

The following chemicals were used for CoO_x film and electrolyte preparations: $Co(NO_3)_2{\cdot}6H_2O$ (≥ 99.999 %, Sigma-Aldrich), l-(+)-Tartaric acid (≥ 99.5 %, Sigma-Aldrich). 2 M NaOH solution (Fisher Scientific), 1 M NaOH solution (Reagecon). Fluorine doped tin oxide (FTO, 25 mm x 25 mm, 2.2 mm in thickness, Ossila). Milli-Q water (resistivity>18.2 MΩ·cm, total organic carbon (TOC) <5 ppb) was used for base dilutions. All chemicals were used without any further treatments, FTO was cleaned twice in ethanol in a sonicator before use.

2.2. Preparation of CoO_x catalyst films

58.214 mg $Co(NO_3)_2{\cdot}6H_2O$ and 300.18 mg l-(+)-Tartaric acid were dissolved in 20 μL of Milli-Q water, and 40 mL of 2 M NaOH aqueous solution was added slowly to it. Tartaric acid was introduced to stabilize Co ions in alkaline media during electrodeposition process[34]. The mixed solution was ready to be used for electrodeposition when its colour changed from light purple to light green.

Electrodeposition was conducted utilizing a Gamry Reference 3000AE potentiostat with two electrodes: the working electrode (WE) of a pre-cleaned FTO substrate and the counter electrode (CE) of a carbon rod (redox.me), both were positioned in a beaker. The FTO substrate was exposed to a 40 mL of the mixed solution containing Co^{2+} ions, with its height adjusted to ensure an electrodeposition area of 6 cm^2. A constant current of 0.15 mA was applied for 1200 s to achieve a charge density of 30 mC cm^{-2}, resulting in the formation of a CoO_x thin film exhibiting a dark yellow colour (Fig. S1). The applied constant current of 0.15 mA was unchanged, by adjusting the electrodeposition time to 200 s, 400 s, 800 s and 2000s, to achieve the charge density of 5 mC cm^{-2}, 10 mC cm^{-2}, 20 mC cm^{-2} and 50 mC cm^{-2}, respectively (Fig. S1).

2.3. Assembly of flow cell

An air compressor (FLPG Plus) was employed to draw ambient air and elevate its pressure to a target of 1.1 bar. This pressurized air was subsequently directed into a pump (Fluigent LineUp), aimed at facilitating the movement of electrolyte contained in a 2 L plastic reservoir. A flow meter (Fluigent Flow Unit), connected via a plastic tubing, was positioned at the outlet of the reservoir to monitor the rate of electrolyte flowing into the flow cell (redox.me SPECTRO-EFC SMA 905). Through

Table 1
Representative cobalt oxide catalysts studied for the OER.

Starting catalysts	Preparation method	Investigated electrolyte	Detection of Co^{4+}	Investigation technique	Investigated (range of) potential of Co^{4+} formation	Spinel (Co_3O_4) detected	Ref.
CoOOH	Electrodeposition	0.1 M KOH	Yes	In situ Raman spectroscopy and in situ Co-K XAS	1.35 V_{RHE}	No	[24]
CoO_x	Electrodeposition	0.1 M KOH	Yes	In situ Raman spectroscopy	1.58 V_{RHE}	No	[23]
CoO_xH_y	Electrodeposition	1.0 M KOH	Yes	In situ Co-K XAS	1.63 V_{RHE}	–	[26]
CoO_x	Electrodeposition	pH 0–14	Yes	Electron paramagnetic resonance	1.63 V_{RHE} at pH 3.4, 1.66 V_{RHE} at pH 7, 1.34 V_{RHE} at pH 13	–	[27]
CoO_x	Commercial CoO_x nanoparticles	0.1 M KOH	Yes	In situ attenuated total reflectance infrared	1.40 V_{RHE}	Yes	[22]
CoO_x	Plasma-enhanced atomic layer deposition	1.0 M KOH	Yes	X-ray photoelectron spectroscopy	1.71 V_{RHE}	Yes	[28]
Co-Pi catalyst	Electrodeposition	0.1 M K_2HPO_4/ KH_2PO_4	Yes	Electron paramagnetic resonance (EPR)	1.55 V_{RHE}	–	[25]
β-$Co(OH)_2$ platelet particles	Wet chemical synthesis	0.1 M KOH	No	Scanning transmission X-ray microscopy, Co-L XAS	0.95–1.90 V_{RHE}	No	[18]
$CoO_x(OH)_y$ nanoparticles	Inverse micelle encapsulation method	0.1 M KOH	No	In situ Co-K XAS	1.00–1.74 V_{RHE}	–	[20]
CoOOH	Sulfurization and electro-oxidation route	1 M KOH	No	Co-K XAS	1.30–1.65 V_{RHE}	Yes	[21]

parameter adjustments via a software (Fluigent OxyGEN), a constant electrolyte flow rate of 2000 μL min^{-1} was established for the current study, modulated by varying the pump pressure. A waste reservoir was situated at the outlet of the flow cell to collect used electrolyte. The assembly of three electrodes, namely the WE comprising the CoO_x film electrodeposited onto a FTO substrate, the CE consisting of the Pt wire (redox.me), and the reference electrode (RE) employing a Hg|HgO|NaOH (1 M, ALS), were carefully placed to the respective position of the flow cell. Subsequently, the flow cell was closed, and each electrode was connected to its respective cable, while optical fibers were connected to the flow cell (Fig. 1a). The lamp (SL1 Tungsten Halogen Lamp, StellarNet Inc) and the detector (StellarNet Inc) were each connected to one of the optical fibers (Fig. 1b). Prior to electrochemical measurements, the flow cell was carefully checked to assess if there was leakage; any significant leakage prompted disassembly and reassembly again until leaks were eliminated or negligible.

For some cases, integration of an O_2 detector was implemented within the aforementioned system to monitor the production of oxygen during the experiments. Briefly, an optical O_2 sensor (PreSens) was affixed within a T-pipe configuration and positioned at the outlet of the flow cell. Adapting the electrode positioning for such measurements necessitated a modification wherein the CE was relocated from the main chamber of the flow cell, instead, a platinum tube was inserted just following the O_2 sensor, serving also as the CE. This separation of the WE and the CE facilitated comprehensive detection of the generated O_2 prior to its reduction by the CE. However, due to the challenge of excessive O_2 bubble formation at elevated potentials, detection of the produced O_2 was limited to potentials below 1.58 V_{RHE}, as confirmed by preliminary assessments.

2.4. Spectroelectrochemical measurements

All electrochemical measurements were conducted employing a computer-controlled potentiostat (Gamry Reference 3000AE) and a flow cell, equipped with three electrodes as previously above. Similarly, UV–Vis absorption spectral measurements were carried out utilizing the aforementioned setups. Electrochemical data were automatically stored during the measurements, whereas manual saving was necessary for optical spectroscopy measurements; the absorbance spectrum was saved upon reaching a steady state (approx. 10 s) at each employed potential. The measurements were conducted within a temperature range of 19.0 to 20.5 °C. Electrolyte with varying OH^- concentrations were prepared by diluting 1 M NaOH aqueous solution prior to measurements. While it is more common in literature to report the pH, we report the OH^- concentration herein which was directly controlled. The conversion to pH and pH measurements can be found in Table S1 of the SI. We note that the roughly estimated pH and the actually measured pH are within 2 units from the pKa of H_2O/OH^- at pH 14 (Table S1). Therefore, the used alkaline solutions are sufficiently proton buffering under the used conditions of low current density. The voltage between the Hg|HgO|NaOH reference electrode and a commercial reversible hydrogen electrode (RHE, HydroFlex®) was measured for 10 min the different electrolytes employed. The last value measured was used to convert the measured potentials to the RHE scale. Briefly, the experimental procedure involved conditioning the catalyst surface through potential cycling for 25 repeats with a scan rate of 50 mV s^{-1} in the potential range of 0.6 V to 1.7 V vs RHE. followed by electrochemical impedance spectroscopy (EIS) at open-circuit in the range 1–280,000 Hz using 10 mV rms excitation to measure the uncompensated resistance (R_u) at open circuit potential between 1 Hz and 280,000 Hz. Subsequently, chronoamperometry (CA) measurements were performed that started from 0.8 V vs RHE and stepwise increased to 1.76 V vs RHE, each applied potential was followed by switching potential down to 0.9 V vs RHE (after 1.1 V), the holding time at each potential was 1 min (the CA measurement protocol is detailed in Fig. S2a). UV–Vis absorbance spectra were recorded at each applied potential during CAs (the one recorded at 0.8 V vs RHE serves as a baseline). Background-corrected absorbance spectra were derived from the difference in absorbance corresponding to each applied potential and 0.9 V measured afterwards (see the detailed measurement protocol shown in Table S2), aiming not only to reduce as much as possible the oxidized Co species to a reduced state at 0.9 V, but also to correct for any shifts of the spectral baseline during the measurements. By using a CA measurement protocol (Fig. S2a), the amount of accumulated the total Co oxidized species (Co^{4+} and Co^{3+}) can be analysed quantitatively in the form of reductive charge by integrating the current spike in Fig. S2b at 0.9 V vs RHE following each applied potential. The detailed spectroelectrochemical measurement protocol can be found in Table S2. The currents corresponding to each applied potential were recorded and averaged over the last 5 s during the 60 s hold (CA measurement), which was utilized to evaluate the OER activity. The ohmic drop, also known as iR_u drop, was post-corrected by subtracting iR_u from the applied potentials, where i represents the measured current and R_u denotes the uncompensated resistance.

2.5. Scanning electron microscopy (SEM)

The morphological characteristics of the CoO_x samples, both prior to and after electrochemical measurements, were analysed using a Zeiss LEO Gemini 1530 scanning electron microscope, with an acceleration voltage of 3 keV in high vacuum. For each sample, five random regions were chosen for analysis at different scales.

2.6. X-ray diffraction (XRD)

The structural characteristics of the substrates and the CoO_x samples,

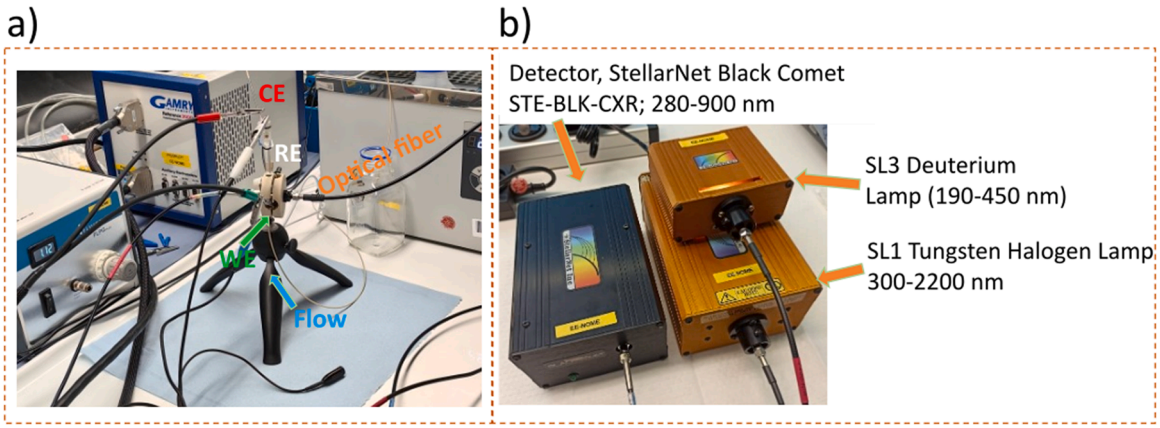

Fig. 1. The pictures of the flow cell equipped with three electrodes (a) and the UV–Vis device (b) employed in the present study.

both prior to and after electrochemical measurements, were analysed with Bruker D8, using Cu K_α irradiation and scanning from 20° to 80°.

2.7. X-ray absorption spectroscopy (XAS)

The XAS measurements of the electrodeposited CoO_x films were conducted at beamline KMC-3 with the CryoEXAFS endstation at BESSY II[36]. The films were made identical to those for the UV–Vis absorption studies except for deposition on glassy carbon instead of FTO. XAS instead of surface-sensitive XPS (X-ray photoelectron spectroscopy) technique was applied due to the porous structure[24] of the CoO_x film that requires bulk methods[37]. Spectra were recorded in fluorescence mode using a 13-element silicon drift detector (SDD) from RaySpec. The used monochromator was a double-crystal Si (111), and the polarization of the beam was horizontal. The energy was calibrated using a Co metal foil (fitted reference energy of 7709 eV in the first derivative spectrum) measured in fluorescence mode (with the detector moved back to avoid saturation) before, intermittent and after the in situ experimental series. Further information may be found in our previous report[38].

The reference spectra of $LiCoO_2$ and Co_3O_4 were recorded in transmission mode using ion chambers at beamline KMC-2 with the XANES endstation at BESSY II[39]. The used double monochromator consisted of two Ge-graded Si(111) crystal substrates and the polarization of the beam was linear horizontal. The energy was calibrated to 7709 eV at the first inflection point using the same Co metal foil as for the CoO_x measurements measured after the sample using another ion chamber. Further information may be found in our previous report[40].

The data refinement was performed using the in-house software BESSY 4.0. The performed operations for XANES and EXAFS data extraction are detailed below. The XAS data were normalized by the subtraction of a 1st order polynomial obtained by fitting the data before the K edge and division by a 2nd order polynomial obtained by fitting the data after the K edge for XANES spectra. For extraction of the EXAFS, a knot spline function with 3 knots was fit to the post-edge and then subtracted to reduce side lobes and artificial peaks at low reduced distance. The as-recorded data were then re-binned to equidistant k-space steps of 0.05 eV and weighted by k^3. The Fourier transform (FT) of the extended X-ray absorption fine structure (EXAFS) was calculated between 25 and 550 eV (2.6 to 12.0 $Å^{-1}$) above the K edge (E0=7709 eV for Co). A cosine window covering 10 % on the left side and 10 % on the right side of the EXAFS spectra was used to further suppress the side lobes of the FTs.

3. Results and discussion

The CoO_x film was electrodeposited on FTO as detailed in the Experimental section. Unless otherwise stated, a charge density of 30 mC cm^{-2} was applied during the electrodeposition process for all CoO_x films preparation in the present study. This charge density was selected to ensure adequate optical signal in the UV–Vis absorbance spectra and to make the most of the CoO_x films deposited on the FTO substrate (Fig. S1). The morphology of the resulting CoO_x film was evaluated via SEM, revealing a uniform film structure with discernible particle-like features distributed across the surface (Fig. S3), which is consistent with the observation of a previous study[24]. The structural analysis of the CoO_x film was conducted using XRD, which predominantly highlights features relevant to the substrates. Specifically, sharp peaks indicative of the crystalline structure of the FTO substrate, while broad humps indicative of glassy carbon substrate (Fig. S4). These two together suggest that the CoO_x films lacks long-range order. Despite the absence of long-range order of the films, the layered CoO_x structure is confirmed via the analysis of Fourier transform (FT) of the EXAFS spectrum at Co-K edge (Fig. S5). The FT is typical for disordered layered (hydr)oxides [41,42]. EXAFS fits of identically prepared samples were discussed previously [34], which support the assignment. The experimental fingerprint of the EXAFS in k-space and its FT also clearly excluded other significant contributions from other phases such as rock salt CoO or spinel Co_3O_4 (Fig. S5).

The redox of the material was probed by CV. Fig. 2 and Fig. S6 presents a general overview of potential-induced Co redox transitions recorded in electrolytes with different OH^- concentrations, illustrating the characteristic voltammograms of CoO_x films featuring three discernible oxidation peaks denoted as I, II, and III. These redox events, according to relevant reports[43,44], are assigned to the successive conversions between $Co^{2+}/Co^{2.x+}$ (the intermediate oxidation state of Co between 2+ and 3+) near peak I, $Co^{2.x+}/Co^{3+}$ near peak II and Co^{3+}/Co^{4+} near peak III. Furthermore, our in situ XAS supports the presence of Co^{2+} at 0.9 V vs RHE and Co^{4+} at 1.6 V vs. RHE in 0.1 M NaOH (Fig. S7). Note that the electrode potentials were not iR_u-compensated, meaning that Co^{4+} likely existed at lower potentials, thus corroborating the assignment of the highest oxidation state to Co^{4+}. Notably, the third oxidation peak of the CVs in Fig. 2, positioned at approximately 1.5 V vs RHE that represents the Co^{3+}/Co^{4+} transition, was shown to exhibit a OH^- concentration-dependent behaviour; at higher OH^- concentration (and thus higher pH), the amplitude of peak III is enhanced, implying the formation of a higher amount of Co^{4+}. Consequently, it is expected that at higher OH^- concentration, a larger portion of oxidized Co^{4+} species, and thus the overall higher oxidation state of Co is observed. By comparison, the redox current observed on a bare FTO substrate is found to be relatively small (the amplified profile can be seen in Fig. S8), indicating minimal influence from the substrate on the Co redox processes.

To track the Co oxidation process in situ, UV–Vis absorption spectroelectrochemical measurements were carried out using a flow cell under conditions with various OH^- concentrations. Fig. S9 and Fig. 3 present representative absorbance spectra and differential absorbance (ΔA) spectra, respectively. Application of a potential of 1.0 V vs RHE leads to the electrochromism of CoO_x catalysts[32,45], which is accompanied by the emergence of a broad absorption band located at around 450 nm (labelled a in Fig. 3a-e). Since negligible spectral changes are visible for a bare FTO substrate upon application of

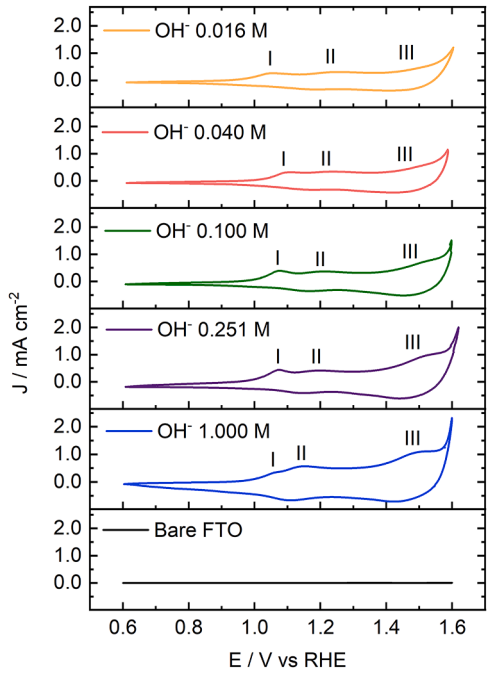

Fig. 2. CVs of CoO_x films electrodeposited onto FTO recorded in electrolytes of different OH^- concentrations. The CV of a bare FTO collected in 0.1 M OH^- electrolyte serves as a reference. A scanning speed of 50 mV s^{-1} was applied for all measurements. All CVs were recorded in the flow cell with a flow rate of 2000 µL min^{-1}.

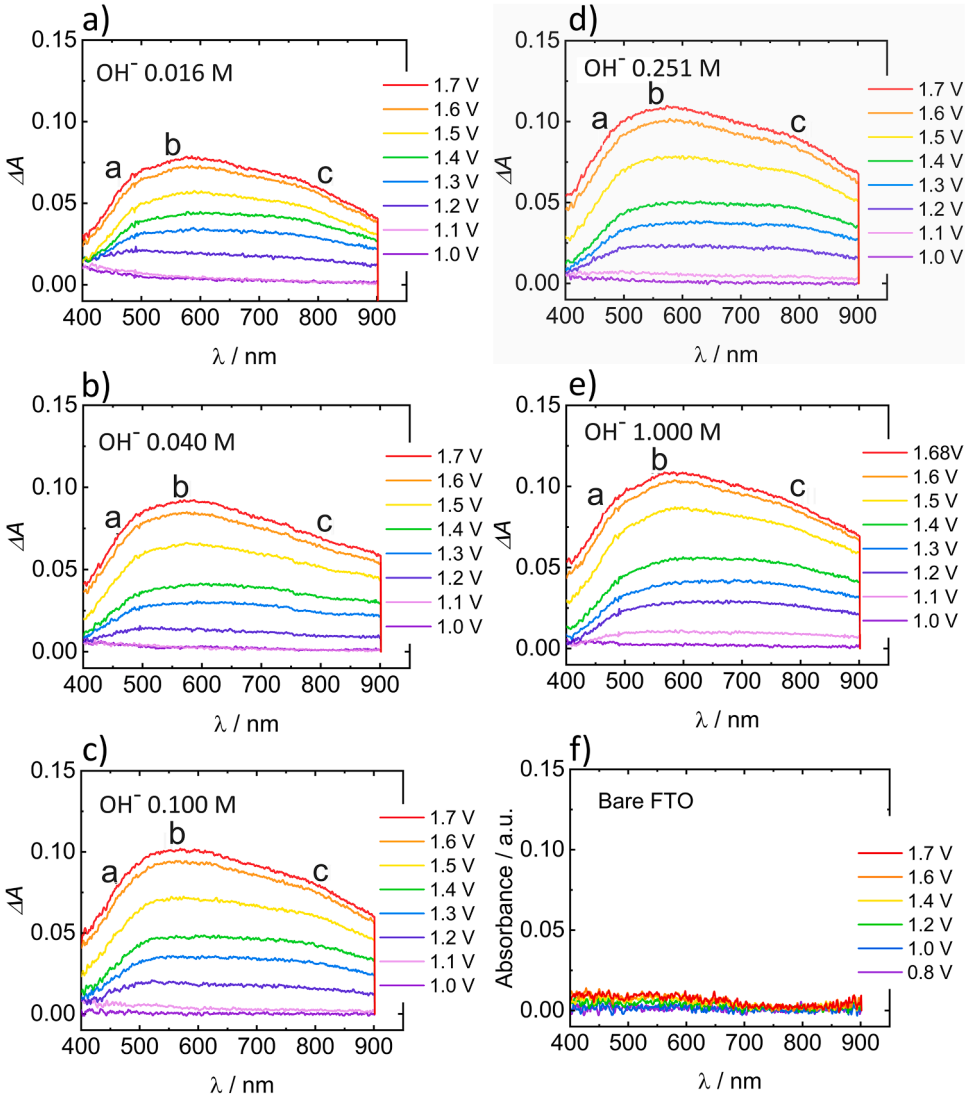

Fig. 3. In situ UV–Vis differential absorbance spectra of CoO_x films as a function of potential recorded in NaOH electrolytes with concentration of OH^- 0.016 M (a), OH^- 0.040 M (b), OH^- 0.100 M (c), OH^- 0.251 M (d) and OH^- 1.000 M (e). The absorbance spectra of a bare FTO (f) collected at 0.1 M NaOH serves as a reference. Prior to each set of measurements, the baseline was measured at 0.8 V vs RHE, where no Co redox occurs. All potentials indicated in the figure are relative to the RHE scale.

potentials (Fig. 3f), the absorbance band at 450 nm was thus attributed to Co^{2+}, which decreases at potentials above peak I in Fig. 2 as expected for the Co^{2+} oxidation.

Upon increasing potential to 1.2 V vs RHE, the absorbance bands evolve to approximately span the entire absorbance regime. Although the wide absorbance bands do not allow for precise positioning of the maximum absorbance, the value of 550 nm (labelled b) and 800 nm (labelled c) were selected because of their relatively high visibility as displayed by absorbance spectra. In general, peaks b and c exhibit a similar evolution with increasing potential, including comparable onset potentials for their appearance and analogous intensification with potential. Therefore, both peaks are attributed to the formation of oxidized Co, i.e., Co^{3+} and Co^{4+}. A quantitative assignment to individual species is beyond this work and requires further experiments, such as those reported elsewhere [46].

Notably, the UV–Vis absorbance spectra generally exhibit heightened intensity in response to increasing OH^- concentration, this is particularly evident for $\lambda_{550\ nm}$ and $\lambda_{800\ nm}$ absorbance bands that are associated with the generation of Co^{3+} and Co^{4+}. This observation is well in agreement with the enhanced oxidation currents depicted by peak III for higher OH^- concentration (Fig. 2). Therefore, based on these analyses, the three broad absorbance bands observed approx. at 450 nm (a), 550 nm (b) and 800 nm (c) were assigned to the presence of Co^{2+} and the combined presence of Co^{3+} and Co^{4+}. This finding suggests that, monitoring of the overall changes in the oxidation states of Co can be qualitatively achieved by using in situ UV–Vis absorption spectroscopy. A previous study on Co-based complexes demonstrated that both Co^{3+} and Co^{4+} species can be detected near 800 nm in UV–Vis spectra, with peak intensity increasing for Co^{4+} compared to Co^{3+}[47]. While similar observations were made in the present study, peak c exhibits a bump at high potential under elevated OH^- concentrations, therefore, peak c was selected for further analysis.

The optical signal of the UV–Vis absorption spectra is proportional to the density of the analyte under investigation[29,31], i.e., the oxidized Co species in this study. Analysis of the differential absorbance at 800 nm as a function of potential across a range of OH^- concentrations reveals a notable trend, wherein absorbance intensity generally increases with OH^- concentration (Fig. 4a), reaching near-constant absorbance at both low (below 1.2 V vs RHE) and high (above approximately 1.57 V vs RHE, Fig. 4b) potential regions. This trend further supports that the absorbance band at 800 nm corresponds to the formation of both Co^{3+} and Co^{4+} species, associated with the redox transitions II and III in

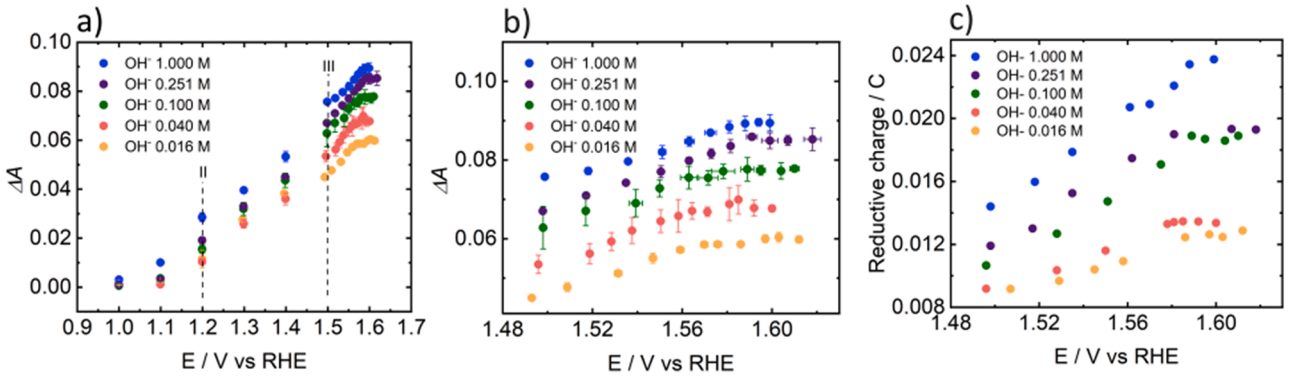

Fig. 4. Absorbance intensity extracted from differential spectra at 800 nm (a, b) and absolute reductive charge of the mixture of Co^{4+} and Co^{3+} at 0.9 V vs RHE (c) following each single applied potential recorded in different OH^- concentrations. The dashed lines II and III in Fig. 4a correspond to the respective redox transition of Co shown in Fig. 2. Fig. 4b shows an enlarged view of Fig. 4a at potential higher than 1.48 V vs RHE. The errors are standard deviations obtained from three freshly prepared electrodes.

Fig. 2, respectively.

Notably, at potentials above 1.57 V vs. RHE, the UV–Vis absorbance approaches saturation, however, the reductive charge continues to rise, particularly at 1 M OH^- (Fig. 4c). This suggests that at higher potential (above 1.57 V), more Co^{4+} forms at elevated OH^- concentrations, contributing to the continued rise in reductive charge. It is more visible in the electrochemical data since Co^{4+} to Co^{2+} reduction creates two electrons, while Co^{3+} to Co^{2+} only creates one electron per reduced Co. In brief, both Co^{3+} and Co^{4+} are detected at $\lambda_{800\ nm}$, with Co^{4+}becoming predominant at potentials exceeding 1.57 V vs RHE, this is particularly pronounced at high OH^- concentrations.

Further analysing the reductive charge as a function of potential (Fig. 4c) in more detail, we found that a near-linear correlation between the reductive charge and applied potentials is established, especially for OH^- concentrations higher than 0.1 M. Furthermore, the reductive charge clearly increases with higher OH^- concentrations at a given potential. Interestingly, the slope of the variation of reductive charge with potential increases with higher OH^-, and in particular the slope increases more significantly for OH^- $\geq$0.1 M compared to that for OH^- <0.1 M. This phenomenon is in good agreement with the visibility of peak III in ~~Figure 1~~ Fig. 2 associated with Co^{3+}/Co^{4+}transition, i.e., peak III becomes more pronounced with higher OH^- concentrations. Therefore, the information provided in Fig. 4c once more suggests that Co^{4+} is more readily formed at higher OH^- concentrations (Co^{3+} may still be formed and detected).

We further elucidated the OER activity of CoO_x in terms of current density and overpotentials under various electrolyte conditions to correlate it with our spectroscopic insights. Firstly, a detectable amount of O_2 is established at approximately 1.54 V vs RHE in 0.1 M OH^- using an optical O_2 detector (Fig. S10). Note that this potential is higher than the onset potential region for the oxidation of Co^{3+} to Co^{4+}in 0.1 M OH^- (indicated by peak III in Fig. 2), which implies that Co^{4+} was present during the OER at the higher potential. Interestingly, we observed that the OH^- concentration-dependent OER activity is contingent upon the applied potential (Fig. 5a). At low overpotentials (approx. below 1.57 V vs RHE), the OER activity remains independent of OH^- concentration, by comparison, at higher overpotentials (approx. 1.57 V vs RHE onwards), the OER activity exhibits a OH^- concentration-dependent behaviour, i.e., the OER activity is promoted by higher OH^- concentration (note that these potentials are on the RHE scale, which means that differences in potential of the reference electrode due to changes of OH^- concentration are already taken into account).

Mechanistic insight was gained from a qualitative evaluation of the reaction orders with respect to reductive charge (Fig. 5b) and OH^- activity (Fig. 5c). The reaction orders were obtained as the slopes in log-log plots. At a potential of 1.54 V vs RHE, we detect O_2 (Fig. S10) and the reaction order with respect to reductive charge and OH^- activity was zero within error. In contrast, we found finite reaction orders with respect to both variables at a higher potential of 1.59 V vs RHE. Therefore, our analysis indicates that the OER on our CoO_x became dependent on OH^- activity and thus pH. The reductive charge relates to Co^{4+} as discussed above. Specifically, Fig. 4b indicates that Co^{3+} does not change much at high potentials (higher than 1.57 V vs RHE), consequently, the observed changes in slope with respect to reductive

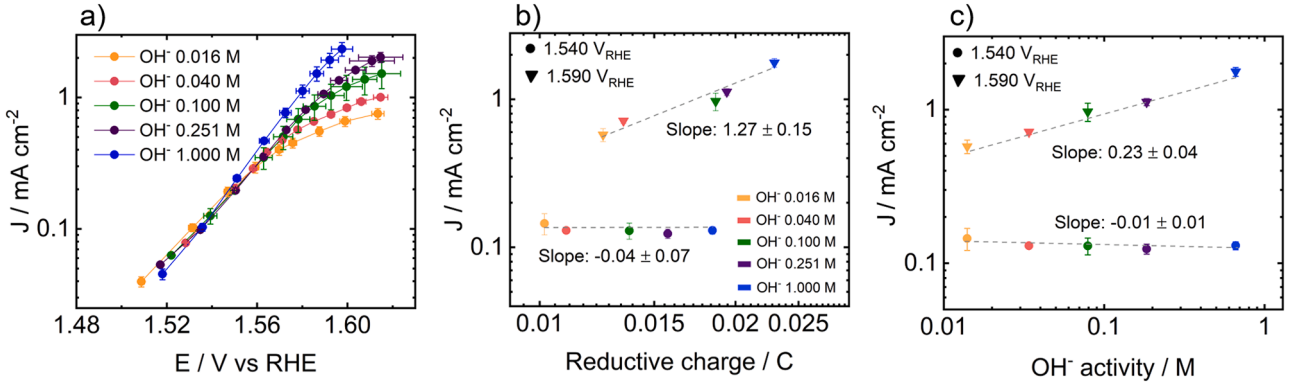

Fig. 5. Comparison of OER activity in terms of current density recorded in NaOH solutions with various OH^- concentrations as a function of potential (a) and reductive charge (b). Reaction order of OH^- ions measured at 1.540 V vs RHE and 1.590 V vs RHE (c). The OER activity was determined from CA measurements, a series of constant potential was applied and the current corresponding to each potential was recorded and averaged over the last 5 s during the 60 s hold. The errors are standard deviations obtained from three freshly prepared electrodes.

charge (Fig. 5b) suggest changes in reaction order with respect to Co^{4+}, this, may enhance the OER activity at high potentials, suggesting that the availability of Co^{4+} limits higher current densities at the higher overpotentials as further discussed below.

We conducted ex situ analyses (Figs. S11, S12) to evaluate the changes of CoO_x films following water electrooxidation. Our results indicated that the CoO_x films exhibit similar characteristics to pristine samples, suggesting minimal changes (i.e., in content of surface Co, in morphology or in bulk structure, respectively) induced by electrochemical processes. Therefore, we propose that the observed differences in OER rates at high overpotentials are primarily attributed to variations in the concentration of accumulated Co^{4+} species with OH^- concentration, i.e., increased OH^- concentrations facilitates Co^{4+} formation, thereby enhancing the OER rates at high overpotentials.

A further plausible explanation for this phenomenon is that as the concentration of OH^- increases, large amounts of Co^{4+} are required as OER active sites to maintain high currents at high overpotentials due to hydroxide oxidation by Co reduction; conversely, at low overpotentials, there is a reduced need for Co^{4+} species, and thus comparable OER performance can be obtained for different OH^- concentrations. Alternatively, at low overpotentials, only a fraction of Co^{4+} can be formed even at high OH^- concentrations, and thus the difference in Co^{4+} density with OH^- concentrations is not sufficient to differentiate the small changes in OER activity[22]. Consequently, the OH^- concentration-dependent OER behaviour at high overpotentials leads to a non-zero reaction order on the RHE scale (Fig. 5c). Potential-dependent changes in reaction order on $CoO_x(OH)_y$ were previously reported[48], which the authors attributed to a difference in water activity from 1.00 to 0.83 leading to a change in reaction pathway. We note that in our work, the water activity remained close to unity (0.999 to 0.966) for the used NaOH concentrations and temperature of near 20 °C (Table S1) [35]; this range of water activities is too narrow to calculate the reaction order with respect to water activity and we thus focus on the role of Co^{4+}.

Numerous investigations have confirmed the presence of Co^{4+} and established its functionality for the OER processes. there are other studies where the presence of Co^{4+} was not observed (Table 1), and instead, Co^{3+} was highlighted for its significance in alkaline OER[14,18,20,21]. There is overlap in the experimental protocols, including electrolyte composition (i.e., OH^- concentration/pH), used electrochemical and characterization methods and detected structures for studies reporting Co^{4+} and those that do not (Table 1). Thus, the discrepancy may stem from the investigated potential range determining the amount of produced Co^{4+} and whether it limits the catalysis under the investigated conditions, in line with a previous hypothesis[48]. We note that rapidly reacting Co^{4+} may not be detected in relatively slow in situ XAS measurements[49]. Furthermore, non-spinel Co oxides, such as the layered structure herein, exhibit greater amorphousness, contain defect sites[50] and have been recognized for Co with oxidation states higher than 3+ serving as active sites for OER, so that it may be more likely to detect Co^{4+} in these materials (e.g. studies in refs. [22–25]). Drawing upon the findings of literature survey, we are more confident that in present study, the amorphous-structured CoO_x films could contain Co^{4+} species, which exerts a crucial impact on the OER activity, particularly at high overpotentials.

4. Conclusions

In summary, we have prepared CoO_x films onto FTO substrates via anodic electrodeposition in alkaline environment, and mainly analysed them through a combination of cyclic voltammetry and in situ UV–Vis absorption spectroscopy to systematically monitor alterations in Co redox states relative to the applied potential in NaOH solutions of different concentrations.

In a qualitative analysis, the onset potential region of the OER and the visibility of the three Co oxidation peaks in CVs exhibit a strong correlation with the observation shown in baseline-corrected absorbance spectra. Particularly, increased electrolyte OH^- concentrations results in amplified signals of oxidative current and optical absorbance associated with Co^{3+} and Co^{4+} formation. Above 1.2 V vs RHE, the absorbance at $\lambda_{800\ nm}$ intensifies with OH^- concentration, suggesting a more pronounced Co oxidation. Above 1.5 V vs RHE, where Co^{4+} is expected from CV, the absorbance approaches as constant value, except for 1.0 M OH^-, while the reductive charge increases. All this suggests the production of Co^{4+} for elevated OH^- concentrations at high potentials (higher than 1.57 V vs RHE).

The reaction orders with respect to OH^- activity and reductive charge both were zero at low OER overpotential and became finite at higher potentials. We argued that the reaction order with respect to reductive charge qualitatively captures the expected trend for the reaction order with respect to Co^{4+}. The change in reaction orders suggest that mechanistic insights at low overpotential are not readily transferable to higher overpotential as also calculated before [19]. We explained the observed correlation by the hypothesis that, at high overpotentials, a higher amount of Co^{4+} is needed as active OER sites to sustain an increased current due to hydroxide oxidation by Co reduction. Consequently, a non-zero OH^- reaction order of the OER on the RHE scale, which already considers changes in the potential of the reference electrode due to differences in OH^- concentration, is achieved in the corresponding regime as the limiting Co oxidation has a distinct dependence on OH^- concentration. In summary, this study reveals the presence of Co^{4+} in the amorphous-structured CoO_x from a spectroscopic point of view, and highlights its significance in improving the basic OER since its availability becomes a clear bottleneck for sustaining high current densities such as used in alkaline electrolyzers.

CRediT authorship contribution statement

Jia Du: Writing – review & editing, Writing – original draft, Validation, Methodology, Investigation, Formal analysis, Data curation. **Joaquín Morales-Santelices:** Writing – review & editing, Methodology, Investigation, Data curation. **Omeshwari Yadorao Bisen:** Writing – review & editing, Investigation, Formal analysis, Data curation. **Denis Antipin:** Writing – review & editing, Investigation, Data curation. **Dulce M. Morales:** Writing – review & editing, Methodology, Investigation. **Marcel Risch:** Writing – review & editing, Writing – original draft, Validation, Supervision, Resources, Project administration, Methodology, Funding acquisition, Formal analysis, Data curation, Conceptualization.

Declaration of competing interest

The authors declare the following financial interests/personal relationships which may be considered as potential competing interests:

Marcel Risch reports financial support was provided by European Research Council. Marcel Risch reports equipment, drugs, or supplies was provided by Bundesministerium für Bildung und Forschung. Marcel Risch reports equipment, drugs, or supplies was provided by German Research Foundation. If there are other authors, they declare that they have no known competing financial interests or personal relationships that could have appeared to influence the work reported in this paper.

Acknowledgements

This project has received funding from the European Research Council (ERC) under the European Union's Horizon 2020 research and innovation program under grant agreement No 804092. We acknowledge support from the German Federal Ministry of Education and Research (BMBF) in the framework of the projects Catlab (03EW0015A/B) and OPERANDO-XAS (05K19KE1) as well as and by the German Research Foundation (DFG,) under Germany's Excellence Strategy—EXC 2008—390540038—UniSysCat. Measurements were carried

out at the KMC-2 and KMC-3 endstations at the BESSY II electron storage ring as well as Correlative Microscopy and Spectroscopy (CCMS) and X-ray core labs, all operated by the Helmholtz-Zentrum Berlin für Materialien und Energie[36,39]. The authors thank Dr. Götz Schuck, Dr. Klaus Schwarzburg and Dr. Michael Tovar for their assistance with XAS, SEM and XRD, respectively, and Dr. Javier Villalobos for discussion. We would like to dedicate this article to Prof. Elena Savinova whose mechanistic studies on electrocatalysts inspired us and keeps inspiring us.

Supplementary materials

Supplementary material associated with this article can be found, in the online version, at doi:10.1016/j.electacta.2024.145489.

Data availability

The data that support the findings of this study are openly available in Zenodo at 10.5281/zenodo.14330841, reference number 14330841.

References

[1] S. Chu, A. Majumdar, Opportunities and challenges for a sustainable energy future, Nature 488 (2012) 294–303, https://doi.org/10.1038/nature11475.
[2] N.T. Suen, S.F. Hung, Q. Quan, N. Zhang, Y.J. Xu, H.M. Chen, Electrocatalysis for the oxygen evolution reaction: recent development and future perspectives, Chem. Soc. Rev. 46 (2017) 337–365, https://doi.org/10.1039/c6cs00328a.
[3] J. Turner, G. Sverdrup, M.K. Mann, P.C. Maness, B. Kroposki, M. Ghirardi, R. J. Evans, D. Blake, Renewable hydrogen production, Int. J. Energy Res. 32 (2008) 379–407, https://doi.org/10.1002/er.1372.
[4] M. Tahir, L. Pan, F. Idrees, X. Zhang, L. Wang, J.J. Zou, Z.L. Wang, Electrocatalytic oxygen evolution reaction for energy conversion and storage: a comprehensive review, Nano Energy 37 (2017) 136–157, https://doi.org/10.1016/j.nanoen.2017.05.022.
[5] M.I. Jamesh, X. Sun, Recent progress on earth abundant electrocatalysts for oxygen evolution reaction (OER) in alkaline medium to achieve efficient water splitting – A review, J. Power. Sources. 400 (2018) 31–68, https://doi.org/10.1016/j.jpowsour.2018.07.125.
[6] C.C.L. McCrory, S. Jung, J.C. Peters, T.F. Jaramillo, Benchmarking heterogeneous electrocatalysts for the oxygen evolution reaction, J. Am. Chem. Soc. 135 (2013) 16977–16987, https://doi.org/10.1021/ja407115p.
[7] E. Antolini, Iridium as catalyst and cocatalyst for oxygen evolution/reduction in acidic polymer electrolyte membrane electrolyzers and fuel cells, ACS. Catal. 4 (2014) 1426–1440, https://doi.org/10.1021/cs4011875.
[8] N. Mamaca, E. Mayousse, S. Arrii-Clacens, T.W. Napporn, K. Servat, N. Guillet, K. B. Kokoh, Electrochemical activity of ruthenium and iridium based catalysts for oxygen evolution reaction, Appl. Catal. B 111–112 (2012) 376–380, https://doi.org/10.1016/j.apcatb.2011.10.020.
[9] S. Cherevko, S. Geiger, O. Kasian, N. Kulyk, J.P. Grote, A. Savan, B.R. Shrestha, S. Merzlikin, B. Breitbach, A. Ludwig, K.J.J. Mayrhofer, Oxygen and hydrogen evolution reactions on Ru, RuO2, Ir, and IrO2 thin film electrodes in acidic and alkaline electrolytes: a comparative study on activity and stability, Catal. Today 262 (2016) 170–180, https://doi.org/10.1016/j.cattod.2015.08.014.
[10] M. Ledendecker, S. Geiger, K. Hengge, J. Lim, S. Cherevko, A.M. Mingers, D. Göhl, G.V. Fortunato, D. Jalalpoor, F. Schüth, C. Scheu, K.J.J. Mayrhofer, Towards maximized utilization of iridium for the acidic oxygen evolution reaction, Nano Res. 12 (2019) 2275–2280, https://doi.org/10.1007/s12274-019-2383-y.
[11] X. Deng, H. Tüysüz, Cobalt-oxide-based materials as water oxidation catalyst: recent progress and challenges, ACS. Catal. 4 (2014) 3701–3714, https://doi.org/10.1021/cs500713d.
[12] C. Huang, P. Qin, Y. Luo, Q. Ruan, L. Liu, Y. Wu, Q. Li, Y. Xu, R. Liu, P.K. Chu, Recent progress and perspective of cobalt-based catalysts for water splitting: design and nanoarchitectonics, Mater. Today Energy 23 (2022), https://doi.org/10.1016/j.mtener.2021.100911.
[13] C. Wei, R.R. Rao, J. Peng, B. Huang, I.E.L. Stephens, M. Risch, Z.J. Xu, Y. Shao-Horn, Recommended practices and benchmark activity for hydrogen and oxygen electrocatalysis in water splitting and fuel cells, Adv. Mater. 31 (2019), https://doi.org/10.1002/adma.201806296.
[14] M.E. Kreider, M.B. Stevens, Material Changes in electrocatalysis: an in situ/operando focus on the dynamics of cobalt-based oxygen reduction and evolution catalysts, ChemElectroChem. 10 (2023), https://doi.org/10.1002/celc.202200958.
[15] A. Foelske, H.H. Strehblow, Structure and composition of electrochemically prepared oxide layers on Co in alkaline solutions studied by XPS, Surfa. Interface Anal. (2002) 125–129, https://doi.org/10.1002/sia.1267.
[16] J. Chivot, L. Mendoza, C. Mansour, T. Pauporté, M. Cassir, New insight in the behaviour of Co-H2O system at 25-150°C, based on revised Pourbaix diagrams, Corros. Sci. 50 (2008) 62–69, https://doi.org/10.1016/j.corsci.2007.07.002.
[17] M. Bajdich, M. García-Mota, A. Vojvodic, J.K. Nørskov, A.T. Bell, Theoretical investigation of the activity of cobalt oxides for the electrochemical oxidation of water, J. Am. Chem. Soc. 135 (2013) 13521–13530, https://doi.org/10.1021/ja405997s.
[18] J.T. Mefford, A.R. Akbashev, M. Kang, C.L. Bentley, W.E. Gent, H.D. Deng, D. H. Alsem, Y.S. Yu, N.J. Salmon, D.A. Shapiro, P.R. Unwin, W.C. Chueh, Correlative operando microscopy of oxygen evolution electrocatalysts, Nature 593 (2021) 67–73, https://doi.org/10.1038/s41586-021-03454-x.
[19] D. Antipin, M. Risch, Calculation of the Tafel slope and reaction order of the oxygen evolution reaction between pH 12 and pH 14 for the adsorbate mechanism, Electrochem. Sci. Adv. 3 (2023), https://doi.org/10.1002/elsa.202100213.
[20] F.T. Haase, A. Bergmann, T.E. Jones, J. Timoshenko, A. Herzog, H.S. Jeon, C. Rettenmaier, B.R. Cuenya, Size effects and active state formation of cobalt oxide nanoparticles during the oxygen evolution reaction, Nat. Energy 7 (2022) 765–773, https://doi.org/10.1038/s41560-022-01083-w.
[21] X. Zhang, H. Zhong, Q. Zhang, Q. Zhang, C. Wu, J. Yu, Y. Ma, H. An, H. Wang, Y. Zou, C. Diao, J. Chen, Z.G. Yu, S. Xi, X. Wang, J. Xue, High-spin Co3+ in cobalt oxyhydroxide for efficient water oxidation, Nat. Commun. 15 (2024), https://doi.org/10.1038/s41467-024-45702-4.
[22] Y. Lin, L. Yu, L. Tang, F. Song, R. Schlögl, S. Heumann, In situ identification and time-resolved observation of the interfacial state and reactive intermediates on a cobalt oxide nanocatalyst for the oxygen evolution reaction, ACS. Catal. 12 (2022) 5345–5355, https://doi.org/10.1021/acscatal.1c05598.
[23] B.S. Yeo, A.T. Bell, Enhanced activity of gold-supported cobalt oxide for the electrochemical evolution of oxygen, J. Am. Chem. Soc. 133 (2011) 5587–5593, https://doi.org/10.1021/ja200559j.
[24] A. Moysiadou, S. Lee, C.S. Hsu, H.M. Chen, X. Hu, Mechanism of oxygen evolution catalyzed by cobalt oxyhydroxide: cobalt superoxide species as a key intermediate and dioxygen release as a rate-determining step, J. Am. Chem. Soc. 142 (2020) 11901–11914, https://doi.org/10.1021/jacs.0c04867.
[25] J.G. McAlpin, Y. Surendranath, M. Dincă, T.A. Stich, S.A. Stoian, W.H. Casey, D. G. Nocera, R.D. Britt, EPR evidence for Co(IV) species produced during water oxidation at neutral pH, J. Am. Chem. Soc. 132 (2010) 6882–6883, https://doi.org/10.1021/ja1013344.
[26] L.J. Enman, M.B. Stevens, M.H. Dahan, M.R. Nellist, M.C. Toroker, S.W. Boettcher, Operando X-Ray Absorption Spectroscopy Shows Iron Oxidation Is Concurrent with Oxygen Evolution in Cobalt–Iron (Oxy)hydroxide Electrocatalysts, Angewandte Chemie - Int. Ed. 57 (2018) 12840–12844, https://doi.org/10.1002/anie.201808818.
[27] J.B. Gerken, J.G. McAlpin, J.Y.C. Chen, M.L. Rigsby, W.H. Casey, R.D. Britt, S. S. Stahl, Electrochemical water oxidation with cobalt-based electrocatalysts from pH 0-14: the thermodynamic basis for catalyst structure, stability, and activity, J. Am. Chem. Soc. 133 (2011) 14431–14442, https://doi.org/10.1021/ja205647m.
[28] M. Favaro, J. Yang, S. Nappini, E. Magnano, F.M. Toma, E.J. Crumlin, J. Yano, I. D. Sharp, Understanding the Oxygen Evolution Reaction Mechanism on CoOx using Operando Ambient-Pressure X-ray Photoelectron Spectroscopy, J. Am. Chem. Soc. 139 (2017) 8960–8970, https://doi.org/10.1021/jacs.7b03211.
[29] C.A. Mesa, E. Pastor, L. Francàs, UV–Vis operando spectroelectrochemistry for (photo)electrocatalysis: principles and guidelines, Curr. Opin. Electrochem. 35 (2022), https://doi.org/10.1016/j.coelec.2022.101098.
[30] W. Kaim, J. Fiedler, Spectroelectrochemistry: the best of two worlds, Chem. Soc. Rev. 38 (2009) 3373–3382, https://doi.org/10.1039/b504286k.
[31] R.R. Rao, S. Corby, A. Bucci, M. García-Tecedor, C.A. Mesa, J. Rossmeisl, S. Giménez, J. Lloret-Fillol, I.E.L. Stephens, J.R. Durrant, Spectroelectrochemical analysis of the water oxidation mechanism on doped nickel oxides, J. Am. Chem. Soc. 144 (2022) 7622–7633, https://doi.org/10.1021/jacs.1c08152.
[32] M. Risch, F. Ringleb, M. Kohlhoff, P. Bogdanoff, P. Chernev, I. Zaharieva, H. Dau, Water oxidation by amorphous cobalt-based oxides: in situ tracking of redox transitions and mode of catalysis, Energy Environ. Sci. 8 (2015) 661–674, https://doi.org/10.1039/c4ee03004d.
[33] M. Gorlin, J.F. De Araujo, H. Schmies, D. Bernsmeier, S. Dresp, M. Gliech, Z. Jusys, P. Chernev, R. Kraehnert, H. Dau, P. Strasser, Tracking catalyst redox states and reaction dynamics in ni-fe oxyhydroxide oxygen evolution reaction electrocatalysts: the role of catalyst support and electrolyte pH, J. Am. Chem. Soc. 139 (2017) 2070–2082, https://doi.org/10.1021/jacs.6b12250.
[34] J. Villalobos, D.M. Morales, D. Antipin, G. Schuck, R. Golnak, J. Xiao, M. Risch, Stabilization of a Mn−Co oxide during oxygen evolution in alkaline media, ChemElectroChem. 9 (2022), https://doi.org/10.1002/celc.202200482.
[35] J.N. Hausmann, B. Traynor, R.J. Myers, M. Driess, P.W. Menezes, The pH of Aqueous NaOH/KOH Solutions: a Critical and Non-trivial Parameter for Electrocatalysis, ACS. Energy Lett. 6 (2021) 3567–3571, https://doi.org/10.1021/acsenergylett.1c01693.
[36] I. Zizak, P. Gaal, The KMC-3 XPP beamline at BESSY II, J. Large-Scale Re. Facil. JLSRF 3 (2017) A123, https://doi.org/10.17815/jlsrf-3-112.
[37] K. Klingan, F. Ringleb, I. Zaharieva, J. Heidkamp, P. Chernev, D. Gonzalez-Flores, M. Risch, A. Fischer, H. Dau, Water oxidation by amorphous cobalt-based oxides: volume activity and proton transfer to electrolyte bases, ChemSusChem. 7 (2014) 1301–1310, https://doi.org/10.1002/cssc.201301019.
[38] J. Villalobos, D. González-Flores, R. Urcuyo, M.L. Montero, G. Schuck, P. Beyer, M. Risch, Requirements for beneficial electrochemical restructuring: a model study on a cobalt oxide in selected electrolytes, Adv. Energy Mater. 11 (2021), https://doi.org/10.1002/aenm.202101737.
[39] D.M. Többens, S. Zander, KMC-2: an X-ray beamline with dedicated diffraction and XAS endstations at BESSY II, J. Large-Scale Res. Facil. JLSRF 2 (2016) A49, https://doi.org/10.17815/jlsrf-2-65.

[40] O.Y. Bisen, M. Baumung, M. Tatzel, C.A. Volkert, M. Risch, Manganese dissolution in alkaline medium with and without concurrent oxygen evolution in LiMn2O4, Energy Adv. 3 (2024) 504–514, https://doi.org/10.1039/d3ya00434a.
[41] J. Villalobos, D. González-Flores, K. Klingan, P. Chernev, P. Kubella, R. Urcuyo, C. Pasquini, M.R. Mohammadi, R.D.L. Smith, M.L. Montero, H. Dau, Structural and functional role of anions in electrochemical water oxidation probed by arsenate incorporation into cobalt-oxide materials, Phys. Chem. Chem. Phys. 21 (2019) 12485–12493, https://doi.org/10.1039/c9cp01754b.
[42] M. Risch, V. Khare, I. Zaharleva, L. Gerencser, P. Chernev, H. Dau, Cobalt-oxo core of a water-oxidizing catalyst film, J. Am. Chem. Soc. 131 (2009) 6936–6937, https://doi.org/10.1021/ja902121f.
[43] I.G. Casella, M. Gatta, Study of the electrochemical deposition and properties of cobalt oxide species in citrate alkaline solutions, J. Electroanal. Chem. 534 (2002) 31–38, https://doi.org/10.1016/S0022-0728(02)01100-2.
[44] B. Guo, T. Li, H. Hu, Anodic deposition of CoOOH films with excellent performance for electrochemical capacitors, J. Appl. Electrochem. 46 (2016) 403–421, https://doi.org/10.1007/s10800-016-0920-x.
[45] W. Zhang, H. Li, E. Hopmann, A.Y. Elezzabi, Nanostructured inorganic electrochromic materials for light applications, Nanophotonics. 10 (2020) 825–850, https://doi.org/10.1515/nanoph-2020-0474.
[46] C. Pasquini, L. D'Amario, I. Zaharieva, H. Dau, Operando Raman spectroscopy tracks oxidation-state changes in an amorphous Co oxide material for electrocatalysis of the oxygen evolution reaction, J. Chem. Phys. 152 (2020) 194202, https://doi.org/10.1063/5.0006306.
[47] F.F. Pfaff, S. Kundu, M. Risch, S. Pandian, F. Heims, I. Pryjomska-Ray, P. Haack, R. Metzinger, E. Bill, H. Dau, P. Comba, K. Ray, An oxocobalt(IV) complex stabilized by Lewis acid interactions with scandium(III) ions, Angewandte Chemie - Int. Ed. 50 (2011) 1711–1715, https://doi.org/10.1002/anie.201005869.
[48] C. Lang, J. Li, K.R. Yang, Y. Wang, D. He, J.E. Thorne, S. Croslow, Q. Dong, Y. Zhao, G. Prostko, G.W. Brudvig, V.S. Batista, M.M. Waegele, D. Wang, Observation of a potential-dependent switch of water-oxidation mechanism on Co-oxide-based catalysts, Chem. 7 (2021) 2101–2117, https://doi.org/10.1016/j.chempr.2021.03.015.
[49] M. Risch, D.M. Morales, J. Villalobos, D. Antipin, What X-Ray absorption spectroscopy can tell us about the active state of earth-abundant electrocatalysts for the oxygen evolution reaction**, Angewandte Chemie - Int. Ed. 61 (2022), https://doi.org/10.1002/anie.202211949.
[50] A. Badruzzaman, A. Yuda, A. Ashok, A. Kumar, Recent advances in cobalt based heterogeneous catalysts for oxygen evolution reaction, Inorganica Chim. Acta 511 (2020), https://doi.org/10.1016/j.ica.2020.119854.